Journal of Operation and Automation in Power Engineering

Vol. XX, No. XX, Dec. 2022, Pages: XXXX (Proofed)

http://joape.uma.ac.ir

Research Paper

Active Disturbance Rejection Control of Push-Pull DC-DC Converter

Belkacem Rahmani [1, *], *Ahmed Belkhiri* [1], *Khaled Ameur* [2], *Mohammed Benmiloud* [2], *Aboubakeur Hadjaissa* [2], *Brahim Khalil Oubbati* [1], *Mohammed Belkhiri* [1], and *Nabil Abouchabana* [2]

[1]*Telecommunication, Signals and Systems Laboratory, University Amar Telidji, Laghouat, Algeria.*
[2]*LACoSERE Laboratory, University Amar Telidji, Laghouat, Algeria.*

Abstract— *This paper proposes a robust active disturbance rejection control (ADRC) scheme for a push–pull DC–DC converter, addressing challenges posed by parameter uncertainties, load variations, and external disturbances. Unlike most existing studies on other converter topologies, this work develops and validates an ADRC controller specifically designed for the push–pull converter. First, the average model of the converter is presented, and then the system's flatness property is used to design an ADRC controller based on a linear extended state observer (LESO) for total disturbance compensation. Next, a Lyapunov-based stability analysis proves the ultimate boundedness of the observer and tracking errors using a separation argument. Simulation and experimental results validate the effectiveness and superior performance of the proposed controller compared to proportional–derivative (PD) and proportional–integral–derivative (PID) controllers under various operating conditions, providing a fair comparison rarely addressed in existing studies, while maintaining the same control loop specifications.*

Keywords—Push-pull converter, active disturbance rejection control, DC-DC converter, extended state observer, uncertainties.

1. INTRODUCTION

The DC–DC push–pull converter is a cornerstone topology in modern power electronics, widely used in renewable energy systems [1], electric vehicle auxiliary units [2], and power supplies [3]. Its popularity originates from key advantages such as galvanic isolation through a center-tapped transformer [4] and high conversion ratios with reduced semiconductor stress [5]. The topology's compact structure and high power density make it particularly suitable for space-constrained isolated applications.

Research on push–pull converters has increasingly explored diverse structural modifications and control strategies aimed at improving efficiency and dynamic performance. For instance, bidirectional core magnetization enabling efficient transformer utilization has been investigated to reduce magnetic losses [6]. Modified converter architectures have demonstrated enhanced step-up and step-down capabilities, emphasizing the versatility of this topology, [7]. Detailed small-signal analysis integrated with PI control has yielded notable improvements in transient behavior and overall efficiency [8]. Furthermore, soft-switching techniques have been investigated to minimize switching losses and electromagnetic interference (EMI). As reported in [9], recent hybrid resonant and soft-switching configurations achieve zero-voltage switching (ZVS) over wide load ranges, thereby enhancing overall system performance.

Received: 26 Aug. 2025
Revised: 27 Oct. 2025
Accepted: 02 Nov. 2025
*Corresponding author:
E-mail: b.rahmani@lagh-univ.dz (B. Rahmani)
DOI: 10.22098/joape.2025.18196.2422

Despite these benefits, the push–pull converter exhibits inherently nonlinear dynamics due to transformer coupling and switching behavior. The presence of leakage inductance, magnetizing inductance variations, and core saturation introduces significant modeling uncertainties that challenge conventional control methods [10]. Additionally, asymmetrical switching operation can induce flux imbalance in the transformer core, potentially causing saturation and efficiency degradation [11]. These effects, compounded by load transients and input voltage fluctuations, often result in overshoot, extended settling times, and degraded dynamic performance.

Push–pull converter control strategies have traditionally employed PID controllers for their simplicity and well established tuning methods. For instance, [5] designed a photovoltaic emulator based on a push–pull converter using a PI controller tuned through frequency-domain analysis, demonstrating effective yet limited adaptability. Similarly, [2] applied state-space averaging and root-locus design, but such fixed-gain techniques remain sensitive to parameter variations. Experimental results have shown that under time-varying parameters, load, and input voltage fluctuations—common in photovoltaic micro-inverters—these controllers exhibit reduced efficiency and stability margins compared to advanced approaches [12]. More recent developments, such as the LQR–ANN-based control of photovoltaic emulators proposed in [1], have achieved superior dynamic performance and steady-state accuracy by integrating learning-based modeling with optimal control. Consequently, researchers have increasingly turned to fuzzy logic, robust, and intelligent control strategies to improve stability under varying conditions, which, however, come with increased computational demands and implementation challenges. Comparative studies in [11] further confirm that such advanced controllers substantially improve photovoltaic system performance while demanding more sophisticated tuning and processing capabilities.

Controlling uncertain and nonlinear systems remains a key

challenge due to unmodeled dynamics, external disturbances, and parameter variations. Adaptive observer-based control approaches have demonstrated strong effectiveness in handling such uncertainties across diverse applications, including flexible robotic systems [13], cooperative manipulators using operator-based uncertainty estimation techniques [14], and biomedical control of HIV infection dynamics [15]. In contrast, Active Disturbance Rejection Control (ADRC) offers a non-adaptive yet highly effective methodology for real-time estimation and rejection of total disturbances [16]. The method employs an extended state observer to reconstruct the total disturbance and a stabilizing control law to ensure robustness without relying on an accurate system model [17].

Power electronic systems, inherently affected by load and source variations, have greatly benefited from ADRC implementations. For instance, improved schemes for non-minimum phase DC–DC boost converters demonstrated superior voltage regulation and transient response using minimal model information [18]. LADRC variants further optimized disturbance rejection in fly-back [19] and full-bridge converters [20], achieving better dynamic and steady-state performance than classical PI control. Practical advancements include an error-based ADRC formulation that simplifies tuning and implementation in buck converters [21], while a cascaded ESO was proposed in [22] to suppress sensor noise in such converters. More recently, deep reinforcement learning has been integrated into ADRC for PMSM control in More Electric Aircraft, enabling adaptive parameter optimization and improved disturbance resilience [23]. Theoretical work has also established the equivalence of ADRC with flat filters, dirty derivative-based PID, and sliding mode control, offering unified insight into modern robust control strategies [24].

Although the integration of flatness principles with ADRC holds strong theoretical potential, a consistent and experimentally validated technique specifically tailored for push–pull converters remains undeveloped. Furthermore, most existing ADRC studies benchmark their performance against conventional PI or PID controllers; however, these comparisons often lack uniform control specifications—such as matched closed-loop response times or control bandwidths—thereby limiting their conclusions to general performance indicators rather than rigorous equivalence under identical dynamic conditions. To address this limitation, this paper presents the following contributions:

1) Formulation of the control problem for the push-pull converter based on its flatness property, establishing a foundation for implementing the ADRC controller.
2) Design of a robust active disturbance rejection controller to achieve precise voltage regulation and enhance resilience against parameter uncertainties and external disturbances.
3) Extensive validation of the proposed control strategy through both simulation and real-time experiments under varying reference voltages, input conditions, and load disturbances.
4) A comparative evaluation with classical output-feedback PID to demonstrate superior transient response, steady-state accuracy, and disturbance rejection for the same control loop specifications, and with PD controllers to show the effect of controller augmentation with the rejection term.

Throughout this paper, the set $\mathcal{B}_{r_i} := \{\mathbf{x} \in \mathbb{R}^n \mid \|\mathbf{x}\| \leq r_i\}$ is defined as a ball of radius r_i, where $r_i \in \mathbb{R}^+$. Furthermore, the set Ω_{α_i} is defined as $\Omega_{\alpha_i} := \{\mathbf{x} \in \mathbb{R}^n \mid \mathcal{V}(\mathbf{x}) \leq \alpha_i\}$, where $\mathcal{V}(\cdot)$ represents a Lyapunov function. The functions $\psi_{\min}(\boldsymbol{A})$ and $\psi_{\max}(\boldsymbol{A})$ denote the minimum and maximum eigenvalues of the matrix $\boldsymbol{A} \in \mathbb{R}^{n\times n}$, respectively. The remainder of this paper is organized as follows: Section 2 presents the model of the push-pull converter, Section 3 explores its flatness, LESO design, ADRC controller design and closed-loop stability analysis, Section 4 discusses simulation and experimental results, and Section 5 concludes the paper with a summary and future research directions.

2. Model of the Push-Pull System

This section presents the average model of the isolated DC-DC push-pull converter, illustrated in Fig. 1.

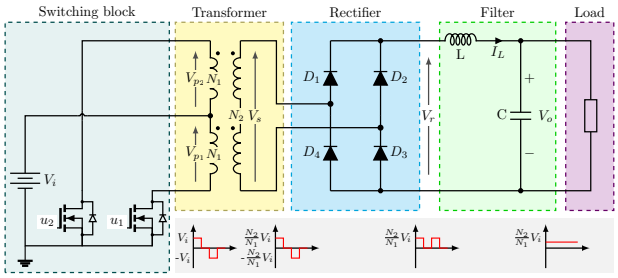

Fig. 1. Push-pull converter circuit.

- *Switching Block:* The switching block generates an AC voltage on the transformer's primary side by switching between the voltage levels $+V_i$, 0, and $-V_i$. The frequency of this AC voltage is determined by the period T of the PWM signal driving the switches u_1 and u_2.
- *High-frequency Transformer:* Let N_1 and N_2 be the number of winding turns in the primary and secondary sides of the transformer. Based on the transformer ratio $\frac{N_2}{N_1}$, the transformer either boosts or reduces the alternating voltage applied to its primary to its secondary side. The transformer output voltage is denoted V_s as in the circuit Fig. 1.
- *Rectifier:* A full-wave bridge rectifier converts the AC voltage V_s to the rectified voltage V_r. The resulting wave has two levels: 0 and $\frac{N_2}{N_1}V_i$.
- *Filter:* A low-pass filter consisting of an inductor (L) and a capacitor (C) is used to smooth out V_r. The block delivers a constant DC output voltage across the resistive R.

The converter operates in two distinct modes; each mode results in a state space model where the states are the voltage across the capacitor (V_o) and the inductor current (I_L).

a) Mode 1: Switch u_1 or u_2 is ON

If either switch u_1 or u_2 is turned ON, energy is transferred from the primary to the secondary circuit; the corresponding model is given by:

$$\begin{cases} \dfrac{dI_L(t)}{dt} = -\dfrac{1}{L}V_o(t) + \dfrac{N_2}{N_1}\dfrac{1}{L}V_i \\ \dfrac{dV_o(t)}{dt} = \dfrac{1}{C}I_L(t) - \dfrac{1}{RC}V_o(t) \end{cases} \tag{1}$$

b) Mode 2: Both switches u_1 and u_2 are OFF

In the case where both switches u_1 and u_2 are OFF, the inductor's stored energy flows freely through the secondary diodes. The state equation is:

$$\begin{cases} \dfrac{dI_L(t)}{dt} = -\dfrac{1}{L}V_o(t) \\ \dfrac{dV_o(t)}{dt} = \dfrac{1}{C}I_L(t) - \dfrac{1}{RC}V_o(t) \end{cases} \tag{2}$$

c) Average model

The push-pull converter is a switched linear system, and its average model is derived by considering the time duration of each mode over one switching period. Mode 1 occurs for a duration of uT, while Mode 2 occurs for $(0.5-u)T$, where u is interpreted as the duty cycle. The average state-space model is given by:

$$\begin{cases} \dfrac{dI_L(t)}{dt} = -\dfrac{1}{L}V_o(t) + \dfrac{2N_2}{N_1}\dfrac{V_i}{L}\left(u(t)+\Delta(t)\right) \\ \dfrac{dV_o(t)}{dt} = \dfrac{1}{C}I_L(t) - \dfrac{1}{RC}V_o(t) \end{cases} \tag{3}$$

where $z(t) = V_o(t)$ represents the output of the system, $u(t)$ is the control input required to operate in the range $0 \leq u(t) \leq 0.5$, and $\Delta(t)$ represents the uncertainty arising from the model averaging process and inherent unmodeled dynamics. The development of this model can be found in [1, 5]. In the following section, the average model is used as the basis for the synthesis of the proposed controller.

3. ADRC CONTROL STRATEGY OF DC-DC PUSH PULL CONVERTER

3.1. Control objectives

Given the desired reference trajectory $z_{ref}(t)$, the main control objective is to ensure that the average output voltage $V_o(t)$ tracks $z_{ref}(t)$ under system uncertainties and disturbances. The following assumption is made:

Assumption 1. The reference trajectories $z_{ref}(t)$, $\dot{z}_{ref}(t)$, and $\ddot{z}_{ref}(t)$ are assumed to be available and bounded.

Reference trajectories can be generated using tracking differentiators, error observers, or reference signal filters. In this work, the filtering approach is adopted to generate reference signals from predefined voltage levels.

3.2. Flatness of the push pull converter

To simplify ADRC design, the converter dynamics are reformulated in terms of the controlled output. Selecting the capacitor voltage as the output renders the system flat. Consider the average model in Eq. (3), and choose $z(t) = V_o(t)$. Using Eq. (3), and taking first and second time derivatives of $z(t)$, we get:

$$\begin{cases} \dot{z}(t) = \dfrac{1}{C} I_L(t) - \dfrac{1}{RC} z(t), \\ \ddot{z}(t) = \dfrac{1}{C} \dfrac{dI_L(t)}{dt} - \dfrac{1}{RC} \dot{z}(t), \end{cases} \tag{4}$$

Substituting $(dI_L(t)/dt)$ from the first state equation in Eq. (3) into Eq. (4) produces:

$$\begin{aligned} \ddot{z}(t) &= \frac{1}{C} \left(-\frac{1}{L} z(t) + \frac{2N_2}{N_1} \frac{V_i}{L} \left(u(t) + \Delta(t) \right) \right) - \frac{1}{RC} \dot{z}(t) \\ &= -\frac{1}{LC} z(t) - \frac{1}{RC} \dot{z}(t) + \frac{2N_2}{N_1} \frac{V_i}{LC} \left(u(t) + \Delta(t) \right) \end{aligned} \tag{5}$$

The quantity $b = \frac{2N_2}{N_1} \frac{V_i}{LC}$, known as the critical input gain, is crucial for achieving the best performance in the ADRC scheme. Notably, only its nominal value is needed to design the controller, as established in [25]. The following section details the design procedure for the proposed controller.

3.3. ADRC controller design

The converter's voltage dynamics in Eq. (5) can be reformulated to include the total disturbance $\delta(t)$, a term that incorporates parametric uncertainties (e.g., input and load variations), unmodeled dynamics, and external disturbances. Let the state variables be $x_1(t) = z(t)$ and $x_2(t) = \dot{z}(t)$. This leads to the state-space model:

$$\begin{aligned} \dot{x}_1(t) &= x_2(t) \\ \dot{x}_2(t) &= \delta(t) + b_0 u(t), \end{aligned} \tag{6}$$

where

$$\delta(t) = -\frac{1}{LC} x_1(t) - \frac{1}{RC} \dot{x}_2(t) + b\Delta(t) + (b - b_0) u(t) \tag{7}$$

represents the total disturbance acting on the system, which includes the mismatch between b and b_0. Here, $b_0 = 2 \frac{N_{2_0}}{N_{1_0}} \frac{V_{i_0}}{L_0 C_0}$ is the nominal value of the input gain b, and the subscript '0' denotes the nominal value of each component. The total disturbance must have a finite rate of change, which leads to the following assumption

Assumption 2. The uncertainty $\delta(t)$ is differentiable, and its derivative is bounded, i.e., $\dot{\delta}(t) = \eta(t)$ with $|\eta(t)| \leq \bar{\eta}$ and $\bar{\eta} \geq 0$.

Following the ADRC design procedure, various observers have been developed for total disturbance estimation, including high-gain and finite-time variants. In this work, a LESO is implemented by augmenting the state vector with the total disturbance $x_3(t) = \delta(t)$ as an additional state:

$$\boldsymbol{x}(t) = \begin{bmatrix} x_1(t) \\ x_2(t) \\ x_3(t) \end{bmatrix} = \begin{bmatrix} z(t) \\ \dot{z}(t) \\ \delta(t) \end{bmatrix}. \tag{8}$$

The augmented state-space model is:

$$\begin{cases} \dot{x}_1(t) = x_2(t) \\ \dot{x}_2(t) = x_3(t) + b_0 u(t) \\ \dot{x}_3(t) = \eta(t) \\ z(t) = x_1(t) \end{cases} \tag{9}$$

The state-space model is expressed in matrix form as:

$$\begin{aligned} \dot{\boldsymbol{x}}(t) &= \boldsymbol{A}\boldsymbol{x}(t) + \boldsymbol{B}u(t) + \boldsymbol{E}\eta(t), \\ z(t) &= \boldsymbol{C}\boldsymbol{x}(t) \end{aligned} \tag{10}$$

where

$$\boldsymbol{A} = \begin{bmatrix} 0 & 1 & 0 \\ 0 & 0 & 1 \\ 0 & 0 & 0 \end{bmatrix}, \quad \boldsymbol{B} = \begin{bmatrix} 0 \\ b_0 \\ 0 \end{bmatrix}, \quad \boldsymbol{E} = \begin{bmatrix} 0 \\ 0 \\ 1 \end{bmatrix}, \quad \boldsymbol{C}^T = \begin{bmatrix} 1 \\ 0 \\ 0 \end{bmatrix} \tag{11}$$

A) Linear extended state observer design

The LESO for the state vector in Eq. (8) is defined for $\hat{\boldsymbol{x}} = \begin{bmatrix} \hat{x}_1 & \hat{x}_2 & \hat{x}_3 \end{bmatrix}^\top$ as:

$$\begin{aligned} \dot{\hat{\boldsymbol{x}}}(t) &= \boldsymbol{A}\hat{\boldsymbol{x}}(t) + \boldsymbol{B}u(t) + \boldsymbol{l}(z(t) - \hat{z}(t)), \\ \hat{z}(t) &= \boldsymbol{C}\hat{\boldsymbol{x}}(t) \end{aligned} \tag{12}$$

where $\boldsymbol{l}$ represents the observer gain vector. Using the standard bandwidth parametrization commonly used in ADRC and found in [26], the observer gains are defined as follows:

$$\boldsymbol{l} = \begin{bmatrix} l_1 \\ l_2 \\ l_3 \end{bmatrix} = \begin{bmatrix} \omega_o \beta_1 \\ \omega_o^2 \beta_2 \\ \omega_o^3 \beta_3 \end{bmatrix} \tag{13}$$

where

$$\beta_i = \frac{(n+1)!}{i!(n+1-i)!}, \quad i = 1, \ldots, 3$$

and ω_0 denotes the observer bandwidth, while β_i are the corresponding binomial coefficients. In the observer formulation, the matrices $\boldsymbol{A}$, $\boldsymbol{B}$, and $\boldsymbol{C}$ are chosen based on the nominal parameter values derived from the system dynamics in Eq. (9), specifically using the nominal input gain b_0. In contrast to other approaches that approximate lumped uncertainties using adaptive control schemes—such as the q-analogue of the Bernstein–Schurer–Stancu operator [14] or the Baskakov operator as a universal approximator [15], where the parameters of the operators are updated via adaptive laws, and the observers are used to estimate tracking errors—our method employs an ESO to directly estimate the lumped uncertainty.

B) Boundedness and convergence of the observer error

The stability of closed-loop nonlinear systems under ADRC has been extensively investigated in the literature [27, 28]. In this paper, a separation analysis is presented to examine the convergence of the observer and tracking errors. Let the observation errors $\tilde{x}_i = x_i - \hat{x}_i$ for $i = 1, 2, 3$ and $\tilde{\boldsymbol{x}} = \begin{bmatrix}\tilde{x}_1 & \tilde{x}_2 & \tilde{x}_3\end{bmatrix}^\top$. It follows that:

$$\dot{\tilde{\boldsymbol{x}}} = (\boldsymbol{A} - \boldsymbol{l}\boldsymbol{C})\tilde{\boldsymbol{x}} + \boldsymbol{E}\eta(t), \tag{14}$$

where:

$$\boldsymbol{A} - \boldsymbol{l}\boldsymbol{C} = \begin{bmatrix} -l_1 & 1 & 0 \\ -l_2 & 0 & 1 \\ -l_3 & 0 & 0 \end{bmatrix} \tag{15}$$

The characteristic equation of the ESO is $\lambda(s) = |s\boldsymbol{I} - (\boldsymbol{A} - \boldsymbol{l}\boldsymbol{C})| = (s + \omega_0)^3$, where the coefficients β_1, β_2, and β_3 inherently satisfy the Hurwitz condition. Therefore, ω_0 is the only tuning parameter. To further analyze the error dynamics, a state transformation is introduced [27]. Let $\boldsymbol{\xi}$ be the vector of the new coordinates and the transformation $\boldsymbol{\xi} = \boldsymbol{\Phi}\tilde{\boldsymbol{x}}$, where:

$$\boldsymbol{\Phi} = \begin{bmatrix} 1 & 0 & 0 \\ 0 & \frac{1}{\omega_o} & 0 \\ 0 & 0 & \frac{1}{\omega_o^2} \end{bmatrix}, \quad \boldsymbol{\xi} = \begin{bmatrix}\xi_1 \\ \xi_2 \\ \xi_3\end{bmatrix}. \tag{16}$$

Substituting the transformed states into the error dynamics, we obtain:

$$\dot{\boldsymbol{\xi}} = \omega_o \boldsymbol{A}_\xi \boldsymbol{\xi} + \boldsymbol{E}\left(\frac{\eta(t)}{\omega_o^2}\right). \tag{17}$$

where

$$\boldsymbol{A}_\xi = \frac{1}{\omega_o}\boldsymbol{\Phi}(\boldsymbol{A} - \boldsymbol{l}\boldsymbol{C})\boldsymbol{\Phi}^{-1} = \begin{bmatrix} -\beta_1 & 1 & 0 \\ -\beta_2 & 0 & 1 \\ -\beta_3 & 0 & 0 \end{bmatrix} \tag{18}$$

Since all eigenvalues of $\boldsymbol{A}_\xi$ are located at -1, the matrix is Hurwitz. Therefore, there exists a positive definite symmetric matrix $\boldsymbol{P}_\xi$ satisfying the Lyapunov equation $\boldsymbol{A}_\xi^\top \boldsymbol{P}_\xi + \boldsymbol{P}_\xi \boldsymbol{A}_\xi = -\boldsymbol{I}$. Consider the following Lyapunov function $\mathcal{V}_o(\boldsymbol{\xi}) = \boldsymbol{\xi}^T \boldsymbol{P}_\xi \boldsymbol{\xi}$, and define an arbitrarily large ball in the error space $\mathcal{B}_{r_o} = \{\, \boldsymbol{\xi} \mid \|\boldsymbol{\xi}\| \le r_o \,\}$ for $r_o > 0$. Let α_o be the minimum value of $\mathcal{V}_o(\boldsymbol{\xi})$ at the edge of Ω_ξ as $\alpha_o = \min_{\|\boldsymbol{\xi}\|=r_o} \mathcal{V}(\boldsymbol{\xi}) = \psi_{min}(\boldsymbol{P}_\xi) r_o^2$. Define the set $\Omega_{\alpha_o} = \{\boldsymbol{\xi} \in \mathcal{B}_{r_o} \mid \mathcal{V}_o(\boldsymbol{\xi}) \le \alpha_o\}$. Now we state the following lemma.

Lemma 1. Provided that the assumption 2 holds, if the $\boldsymbol{\xi}(0) \in \Omega_{\alpha_o}$ then there exists ω_o and finite time T_μ such that the estimation error is upper-bounded by:

$$\begin{aligned} \|\boldsymbol{\xi}(t)\| &\le \sqrt{\frac{\psi_{max}(\boldsymbol{P}_\xi)}{\psi_{min}(\boldsymbol{P}_\xi)}}\, \|\boldsymbol{\xi}(0)\|\, e^{-\left(\omega_o/4\psi_{max}(\boldsymbol{P}_\xi)\right)t} \quad \forall \quad 0 \le t < T_\mu \\ \|\boldsymbol{\xi}(t)\| &\le \sqrt{\frac{\psi_{max}(\boldsymbol{P}_\xi)}{\psi_{min}(\boldsymbol{P}_\xi)}}\, \mu \quad \forall \quad t \ge T_\mu \end{aligned} \tag{19}$$

where $\mu = 4\psi_{\max}(\boldsymbol{P}_\xi)\frac{\bar{\eta}}{\omega_o^3}$. Furthermore, the bound on the disturbance estimation error $\tilde{\delta}(t) = \tilde{x}_3(t)$ is given by

$$|\tilde{x}_3(t)| \le \bar{\delta}, \quad \forall\, t \ge T_\mu \tag{20}$$

where $\bar{\delta} = 4\psi_{\max}(\boldsymbol{P}_\xi)\frac{\bar{\eta}}{\omega_o}$.

Proof. Take the time derivative of the Lyapunov function $\mathcal{V}_o(\boldsymbol{\xi})$:

$$\begin{aligned} \dot{\mathcal{V}}_o(\boldsymbol{\xi}) &= \dot{\boldsymbol{\xi}}^T \boldsymbol{P}_\xi \boldsymbol{\xi} + \boldsymbol{\xi}^T \boldsymbol{P}_\xi \dot{\boldsymbol{\xi}} \\ &= -\omega_0 \boldsymbol{\xi}^T \boldsymbol{\xi} + 2\boldsymbol{\xi}^T \boldsymbol{P}_\xi \boldsymbol{E}\frac{\eta}{\omega_o^n} \\ &\le -\omega_o \|\boldsymbol{\xi}\|^2 + 2\|\boldsymbol{\xi}\|\psi_{\max}(\boldsymbol{P}_\xi)\,\|\boldsymbol{E}\|\,\frac{\bar{\eta}}{\omega_o^n}. \end{aligned}$$

Hence, $\dot{\mathcal{V}}_o(\boldsymbol{\xi}) < -\frac{1}{2}\omega_o\|\boldsymbol{\xi}\|^2$ requires that $\|\boldsymbol{\xi}\| > \mu$, where $\mu = 4\psi_{\max}(\boldsymbol{P}_\xi)\frac{\bar{\eta}}{\omega_o^3}$. This implies that $\mathcal{V}_o(\boldsymbol{\xi})$ is negative outside of the compact set $\mathcal{B}_\mu = \{\boldsymbol{\xi} \mid \|\boldsymbol{\xi}\| \le \mu\}$. Choose $\varepsilon_o = \max_{\|\boldsymbol{\xi}\|=\mu} \mathcal{V}_o(\boldsymbol{\xi}) = \psi_{max}(\boldsymbol{P}_\xi)\mu^2$ and introduce the set $\Omega_{\varepsilon_o} = \{\boldsymbol{\xi} \in \mathcal{B}_r \mid \mathcal{V}_o(\boldsymbol{\xi}) \le \varepsilon_o\}$. From the definition of Ω_{α_o} and Ω_{ε_o} we conclude that $\Omega_{\varepsilon_o} \subset \Omega_{\alpha_o}$. Using [29, Theorem 4.5], we conclude that:

$$\|\boldsymbol{\xi}(t)\| \le \sqrt{\frac{\psi_{max}(\boldsymbol{P}_\xi)}{\psi_{max}(\boldsymbol{P}_\xi)}}\max\left\{\|\boldsymbol{\xi}(0)\|\, e^{-\left(\omega_o/4\psi_{max}(\boldsymbol{P}_\xi)\right)t}, \mu\right\} \tag{21}$$

If $\boldsymbol{\xi}(0) \in \Omega_{\alpha_o}$, then there exists a time $T_\mu \ge 0$ such that the state $\boldsymbol{\xi}(t)$ enters the smaller compact set Ω_{ε_o} at time T_μ at an exponential rate and remains there for all subsequent time. We can immediately deduce the bounds:

$$|\tilde{x}_i(t)| \le |\xi_i(t)|\,\omega_o^{i-1} \le 4\psi_{\max}(\boldsymbol{P}_\xi)\frac{\bar{\eta}}{\omega_o^{4-i}}, \quad \forall\, t \ge T_\mu, \quad i = 1, 2, 3.$$

3.4. ADRC control law

Using the estimate $\hat{x}_3(t) = \hat{\delta}(t)$ from Eq. (12), the control law for simultaneous disturbance rejection and stabilization is defined as:

$$u(t) = \frac{1}{b_0}\left(u_0(t) - \hat{x}_3(t)\right), \tag{22}$$

Substituting this control input reduces the push–pull converter dynamics to an approximate second-order pure integrator.

$$\ddot{z}(t) \approx u_0(t), \tag{23}$$

The nominal component $u_0(t)$ corresponds to a PD controller with a feed-forward term:

$$u_0(t) = -K_p\left(z(t) - z_{ref}(t)\right) - K_d\left(\dot{z}(t) - \dot{z}_{ref}(t)\right) + \ddot{z}_{ref}, \tag{24}$$

where K_p and K_d are the controller gains, determined via bandwidth parametrization based on $s^2 + K_d s + K_p = (s + \omega_c)^2$, with ω_c denoting the controller bandwidth. Accordingly, the gains are $K_p = \omega_c^2$ and $K_d = 2\omega_c$.

□

3.5. Closed loop stability analysis

This section analyzes the stability of the proposed controller. The error dynamics of the closed loop system are derived by defining the following error vector:

$$\boldsymbol{\varepsilon}(t) = \begin{bmatrix}\varepsilon(t) \\ \dot{\varepsilon}(t)\end{bmatrix} = \begin{bmatrix} z(t) - z_{ref}(t) \\ \dot{z}(t) - \dot{z}_{ref}(t)\end{bmatrix}. \tag{25}$$

The error dynamics of the feedback loop are described by:

$$\dot{\boldsymbol{\varepsilon}}(t) = \boldsymbol{A}_\varepsilon \boldsymbol{\varepsilon}(t) + \boldsymbol{B}_\varepsilon(\delta(t) - \hat{\delta}(t)) = \boldsymbol{A}_\varepsilon \boldsymbol{\varepsilon}(t) + \boldsymbol{B}_\varepsilon \tilde{\delta}(t), \tag{26}$$

where:

$$\boldsymbol{A}_\varepsilon = \begin{bmatrix} 0 & 1 \\ -K_p & -K_d \end{bmatrix}, \quad \boldsymbol{B}_\varepsilon = \begin{bmatrix}0 \\ 1\end{bmatrix} \tag{27}$$

and $\tilde{\delta}(t) = \tilde{x}_3$. Since the matrix $\boldsymbol{A}_\varepsilon$ is Hurwitz by definition, there exist positive definite matrices $\boldsymbol{P}_\varepsilon$ and $\boldsymbol{Q}_\varepsilon$ such that $\boldsymbol{A}_\varepsilon^\top \boldsymbol{P}_\varepsilon + \boldsymbol{P}_\varepsilon \boldsymbol{A}_\varepsilon = -\boldsymbol{Q}_\varepsilon$. Define on the tracking error space the Lyapunov function $\mathcal{V}_c(\boldsymbol{\varepsilon}) = \boldsymbol{\varepsilon}^T \boldsymbol{P}_\varepsilon \boldsymbol{\varepsilon}$. Consider an arbitrarily large

ball $\mathcal{B}_{r_c} = \{\ \boldsymbol{\varepsilon} \mid \|\boldsymbol{\varepsilon}\| \leq r_c\ \}$, and set $\alpha_c = \min_{\|\boldsymbol{\varepsilon}\|=r_c} \mathcal{V}_c(\boldsymbol{\varepsilon}) = \psi_{min}(\boldsymbol{P}_\varepsilon) r_c^2$. Let $\Omega_{\alpha_c} = \{\boldsymbol{\varepsilon} \in \mathcal{B}_{r_c} \mid \mathcal{V}_c(\boldsymbol{\varepsilon}) \leq \alpha_c\}$. The main theorem is now stated as follows.

Theorem 1. Consider the system Eq. (6) with the control laws Eq. (22) and Eq. (24). If $\omega_o > \omega_c$, and $\boldsymbol{\varepsilon}(0) \in \Omega_{\alpha_c}$ then there exists finite time T_ρ after which the tracking error is ultimately bounded by:

$$\begin{aligned} \|\boldsymbol{\varepsilon}(t)\| &\leq \sqrt{\frac{\psi_{max}(\boldsymbol{P}_\varepsilon)}{\psi_{min}(\boldsymbol{P}_\varepsilon)}}\, \|\boldsymbol{\varepsilon}(0)\|\, e^{-(\psi_{\min}(\boldsymbol{Q}_\varepsilon)/4\psi_{max}(\boldsymbol{P}_\varepsilon))t} \quad \forall \quad 0 \leq t \leq T_\rho \\ \|\boldsymbol{\varepsilon}(t)\| &\leq \sqrt{\frac{\psi_{max}(\boldsymbol{P}_\varepsilon)}{\psi_{min}(\boldsymbol{P}_\varepsilon)}}\, \rho \quad \forall \quad t \geq T_\rho \end{aligned} \tag{28}$$

where $\rho = 4\frac{\psi_{max}(\boldsymbol{P}_\varepsilon)}{\psi_{min}(\boldsymbol{Q}_\varepsilon)}\bar{\delta}$.

Proof. Take the time derivative of the Lyapunov function $\mathcal{V}_c(\boldsymbol{\varepsilon})$:

$$\begin{aligned} \dot{\mathcal{V}}_c(\boldsymbol{\varepsilon}) &= \dot{\boldsymbol{\varepsilon}}^T \boldsymbol{P}_\varepsilon \boldsymbol{\varepsilon} + \boldsymbol{\varepsilon}^T \boldsymbol{P}_\varepsilon \dot{\boldsymbol{\varepsilon}} \\ &= -\boldsymbol{\varepsilon}^T \boldsymbol{Q}_\varepsilon \boldsymbol{\varepsilon} + 2\boldsymbol{\varepsilon}^T \boldsymbol{P}_\varepsilon \boldsymbol{B}_\varepsilon \tilde{\delta}(t). \end{aligned} \tag{29}$$

Using the bound $\left|\tilde{\delta}(t)\right| \leq \bar{\delta}$, we get:

$$\dot{\mathcal{V}}_c(\boldsymbol{\varepsilon}) \leq -\psi_{\min}(\boldsymbol{Q}_\varepsilon)\|\boldsymbol{\varepsilon}\|^2 + 2\|\boldsymbol{P}_\varepsilon\|\|\boldsymbol{B}_\varepsilon\|\|\boldsymbol{\varepsilon}\|\bar{\delta}. \tag{30}$$

Hence, $\dot{\mathcal{V}}_c(\boldsymbol{\varepsilon}) \leq -\frac{1}{2}\psi_{\min}(\boldsymbol{Q}_\varepsilon)\|\boldsymbol{\varepsilon}\|^2$, if $\|\boldsymbol{\varepsilon}\| > \rho$ where :

$$\rho = 4\frac{\psi_{max}(\boldsymbol{P}_\varepsilon)}{\psi_{\min}(\boldsymbol{Q}_\varepsilon)}\bar{\delta}. \tag{31}$$

Following the same argument as the previous section, we define the set $\mathcal{B}_\rho = \{\boldsymbol{\varepsilon} \in \Omega_{\alpha_c} \ | \|\boldsymbol{\varepsilon}\| \leq \rho\}$ within which $\mathcal{V}_c(\boldsymbol{\varepsilon})$ is negative outside its boundary. Choose $\varepsilon_c = \max_{\|\boldsymbol{\varepsilon}\|=\rho} \mathcal{V}_c(\boldsymbol{\varepsilon}) = \psi_{max}(\boldsymbol{P}_\varepsilon)\rho^2$ and let the set $\Omega_{\varepsilon_c} = \{\boldsymbol{\varepsilon} \in \mathcal{B}_r \mid \mathcal{V}_c(\boldsymbol{\varepsilon}) \leq \varepsilon_c\}$. The definition of Ω_{α_c} and Ω_{ε_c} implies $\Omega_{\varepsilon_c} \subset \Omega_{\alpha_c}$. Then, from [29, Theorem 4.5], we have that:

$$\|\boldsymbol{\varepsilon}(t)\| \leq \sqrt{\frac{\psi_{max}(\boldsymbol{P}_\varepsilon)}{\psi_{max}(\boldsymbol{P}_\varepsilon)}}\, \max\left\{\|\boldsymbol{\varepsilon}(0)\|\, e^{-(\psi_{\min}(\boldsymbol{Q}_\varepsilon)/4\psi_{max}(\boldsymbol{P}_\varepsilon))t}, \rho\right\} \tag{32}$$

If $\boldsymbol{\varepsilon}(0) \in \Omega_{\alpha_c}$, then $\boldsymbol{\varepsilon}(t)$ converges exponentially to Ω_{ε_c} in finite time $T_\rho \geq 0$ and remains there for all $t \geq T_\rho$.

□

Remark 1. From the Lyapunov analysis, it follows that the boundedness of the closed-loop error signals requires $T_\mu < T_\rho$. This condition is guaranteed by selecting a sufficiently large ω_o such that:

$$T_\mu \stackrel{\text{def}}{=} \frac{4\psi_{\max}(P_\xi)}{\omega_o} \ln\left(\frac{\|\boldsymbol{\xi}(0)\|}{\mu}\right) \leq \frac{1}{2}T_\rho. \tag{33}$$

The observer's convergence time $T_\mu(\omega_o)$ depends on the bandwidth. Since:

$$\lim_{\omega_o \to \infty} T_\mu(\omega_o) = \lim_{\omega_o \to \infty} \frac{4\psi_{\max}(P_\xi)}{\omega_o} \ln\left(\frac{\|\boldsymbol{\xi}(0)\|}{\mu}\right) = 0, \tag{34}$$

then the left-hand side of the inequality in Eq. (33) tends to zero as $\omega_o \to \infty$. Therefore, a sufficiently large ω_o satisfying the condition always exists.

4. Simulation and Experimental Results

This section presents simulation and experimental results comparing the proposed ADRC with a PID-like and PD controllers under various operating conditions, including reference tracking, input voltage, and load variations. For fair comparison, the PID controller is designed via state-space pole placement to meet the same control objectives as the ADRC.

4.1. PID controller for comparison

Consider the system in Eq. (5) and define $\sigma_1(t) = z(t)$, $\sigma_2(t) = \dot{z}(t)$. To ensure zero steady-state error for a constant set-point z_{ref}, introduce an integral state $\sigma_3(t) = \int_0^t (\sigma_1(\tau) - z_{ref})\ d\tau$. The augmented state vector is $\boldsymbol{\sigma}(t) = \begin{bmatrix}\sigma_1(t) & \sigma_2(t) & \sigma_3(t)\end{bmatrix}^T$ and the new state equation is defined as follows:

$$\dot{\boldsymbol{\sigma}}(t) = \tilde{\boldsymbol{A}}\boldsymbol{\sigma}(t) + \tilde{\boldsymbol{B}}u(t) + \tilde{\boldsymbol{E}}z_{ref} \tag{35}$$

where

$$\tilde{\boldsymbol{A}} = \begin{bmatrix} 0 & 1 & 0 \\ -\frac{1}{LC} & -\frac{1}{RC} & 0 \\ 1 & 0 & 0 \end{bmatrix}, \quad \tilde{\boldsymbol{B}} = \begin{bmatrix} 0 \\ \frac{2N_2}{N_1}\frac{V_i}{LC} \\ 0 \end{bmatrix}, \quad \tilde{\boldsymbol{E}} = \begin{bmatrix} 0 \\ 0 \\ -1 \end{bmatrix}. \tag{36}$$

The control input is $u(t) = -\tilde{\boldsymbol{K}}\boldsymbol{\sigma}(t)$, where $\tilde{\boldsymbol{K}} = \begin{bmatrix}\tilde{K}_1 & \tilde{K}_2 & \tilde{K}_3\end{bmatrix} \in \mathbb{R}^{1\times 3}$ represents the controller gain vector. To achieve similar control requirement of the proposed ADRC controller, the PID control input is designed such that the characteristic equation satisfies $\lambda(s) = \left|s\boldsymbol{I} - (\tilde{\boldsymbol{A}} - \tilde{\boldsymbol{B}}\tilde{\boldsymbol{K}})\right| = (s + \omega_c)^3$.

4.2. System specifications and design parameters

In this section, we provide the detailed specifications of the push-pull DC-DC converter used in this study, along with the design parameters for the proposed ADRC controller.

A) Reference signal generation

The smooth reference trajectories $z_{ref}(t)$, $\dot{z}_{ref}(t)$, and $\ddot{z}_{ref}(t)$ are generated using a second-order low-pass filter $H(s) = \omega_f^2 / \left(s^2 + 2\zeta\omega_f s + \omega_f^2\right)$ where ω_f is the bandwidth frequency and ζ is the damping coefficient. The filter smooths step inputs, which verifies assumption 1.

B) Converter specifications

The physical parameters of the push-pull converter are summarized in Table 1:

Table 1. Push-Pull converter specifications.

Parameter	Value
Input voltage (V_{i_0})	50 V
Output voltage (V_o)	25 V
Transformer turns ratio (N_{2_0}/N_{1_0})	0.55
Inductance (L_0)	700 μH
Capacitance (C_0)	1360 μF
Load resistance (R_0)	10 Ω
Switching frequency (f_{sw})	25 kHz

C) Controller design parameters

The ADRC controller is designed with the following parameters summarized in Table 2:

Table 2. ADRC controller design parameters.

Parameter	Value
Filter cutoff frequency (ω_f)	1000 rad/s
Filter damping coefficient (ζ)	1
Controller bandwidth (ω_c)	600 rad/s
Observer bandwidth (ω_o)	5000 rad/s
Binomial coefficients ($\beta_1,\ \beta_2,\ \beta_3$)	(3, 3, 1)

Using Eq. (24), the resulting PD gains are $K_p = 360000$ and $K_d = 1200$. Since these gains are divided by b_0 in Eq. (22), the effectively applied gains are $\frac{K_p}{b_0} = 62 \times 10^{-4}$ and $\frac{K_d}{b_0} = 2.0771 \times 10^{-5}$. For the output PID controller defined in Eq. (36), the pole placement method yields the gains $\tilde{K}_1 = 5.12 \times 10^{-4}$, $\tilde{K}_2 = 2.9884 \times 10^{-5}$, and $\tilde{K}_3 = 3.7388$.

D) Simulation and experimental setup

The simulation and experimental tests are conducted through 3 different scenarios, namely, trajectory tracking, regulation subject to input voltage variations, regulation under load changes. The following conditions are considered, as summarized in Table 3:

The input and load variations are generated using programmable DC sources and loads, following repeated sequences specified in Table 3.

The experimental setup shown in Fig. 2 includes a push-pull converter, a LAUNCHXL-F28379D microcontroller (TMS320F28379D, Texas Instruments), and associated voltage and current sensing and control circuitry.

The sampling frequency for the control loop was set to $f_s = 100\,\text{kHz}$, ensuring high-resolution control and effective disturbance rejection.

Table 3. Simulation and experimental conditions.

Scenarios	Range
Reference signal step values (S1)	5, 12.5, 15, 20, 25 V
Input voltage variation (S2) ($z_{ref} = 12.5$ V)	50, 40 V
Load variation (S3) ($z_{ref} = 12.5$ V)	10, 12.5, 15, 20, 25 Ω

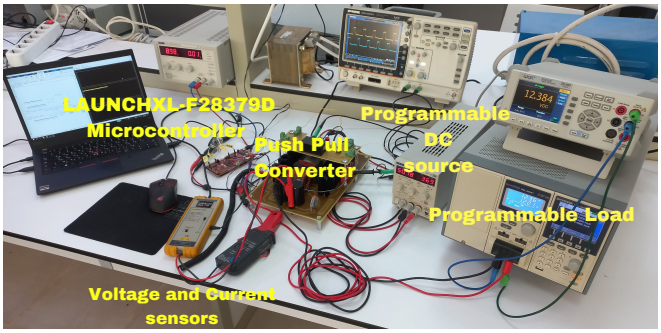

Fig. 2. Laboratory setup for the implementation of the ADRC controller.

4.3. Simulation results

Fig. 3 illustrates the output voltage tracking across three phases: initial tracking (0–4 s), input voltage variation (4–6 s), and load variation (6–8 s), as defined in Table 3. Compared to the PID controller, ADRC provides a fast, smooth, and overshoot-free response, while the PD controller exhibits poor tracking. Under input voltage variation, ADRC maintains the reference with minimal deviation, unlike the PID controller, which shows noticeable overshoot. During load variation, ADRC rapidly restores voltage regulation, whereas PD and PID controllers show larger transients and slower recovery.

Fig. 4 illustrates the tracking error, confirming the expected behavior observed previously. Fig. 5 depicts the control inputs, showing that the ADRC achieves faster control actions compared to the PD and PID controllers.

4.4. Experimental results

The experimental results compare the proposed ADRC against PID and PD controllers. Performance is shown in separate voltage/current and tracking error/control effort figures.

A) Scenario 1:

The first scenario evaluates the tracking of dynamic reference voltage levels.

B) Scenario 2

The second scenario tests the system's rejection of input voltage disturbances.

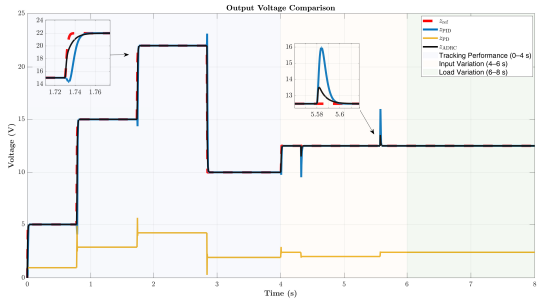

Fig. 3. Simulated output voltage comparison, demonstrating ADRC's superior tracking and disturbance rejection over PID and PD.

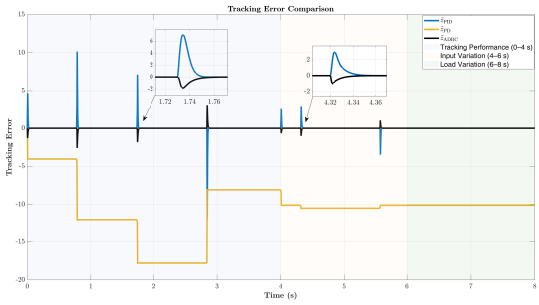

Fig. 4. Simulated comparative tracking errors, highlighting ADRC's minimal deviation across all test scenarios.

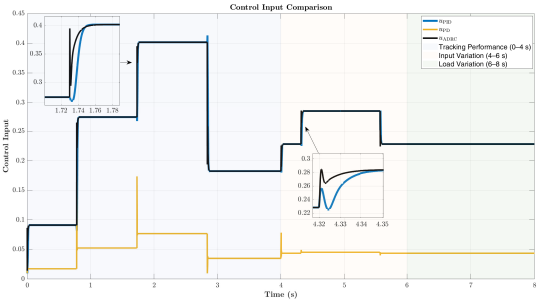

Fig. 5. Control effort comparison in simulation, showing ADRC's active disturbance compensation during transients.

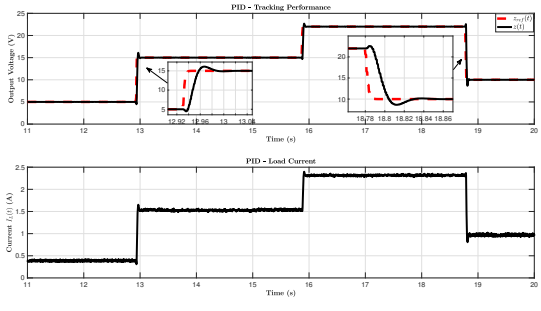

Fig. 6. Experimental PID response to a varying reference step levels, showing output voltage and inductor current.

C) Scenario 3

The final scenario assesses the output voltage regulation under step load changes.

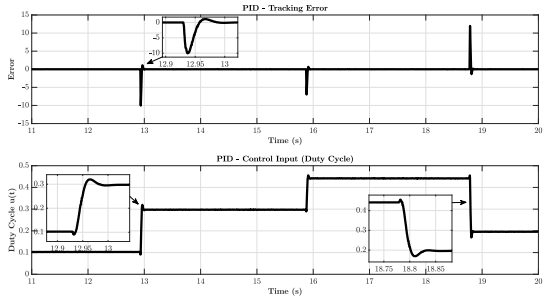

Fig. 7. PID tracking error and control signal, revealing steady-state performance and control reaction.

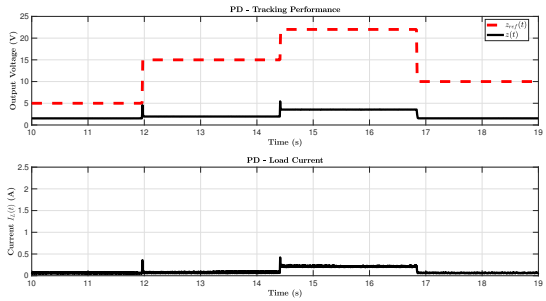

Fig. 8. Voltage and current response of the PD controller during tracking performance, revealing poor tracking accuracy and steady-state deviation.

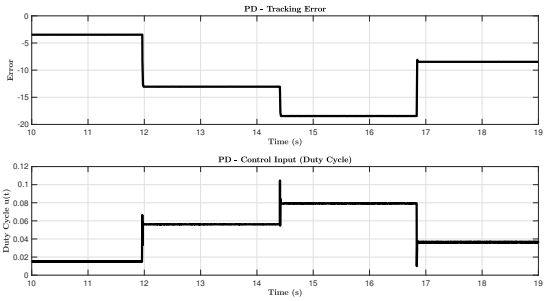

Fig. 9. PD tracking error and control effort during the step change..

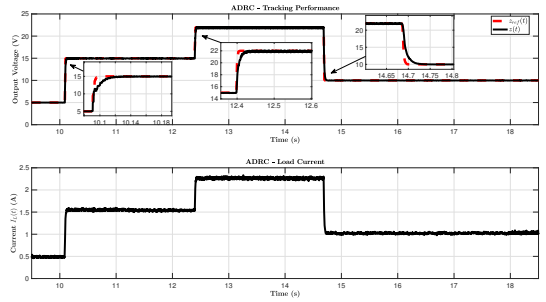

Fig. 10. ADRC experimental tracking performance, demonstrating fast and accurate reference following.

D) Comparative performance analysis

For a comprehensive assessment, a quantitative comparison of the three controllers is presented in Table 4. Standard performance indices—IAE, ISE, ITAE, settling time, and percent overshoot—are computed from the experimental results to evaluate the three controllers.

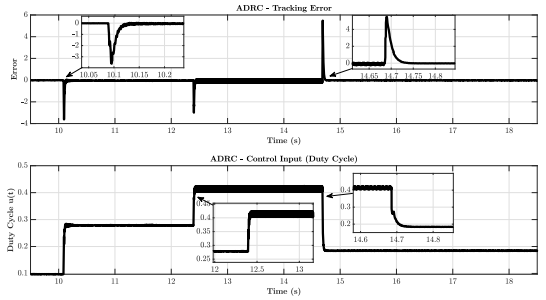

Fig. 11. ADRC's minimal tracking error and corresponding control input.

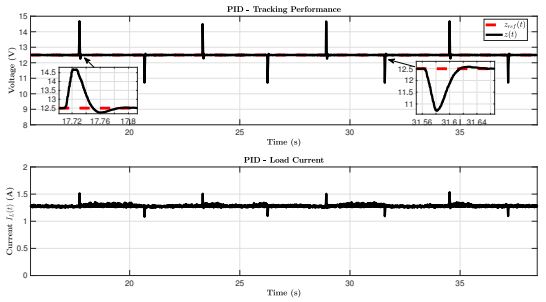

Fig. 12. Voltage and current response of the PID controller under input voltage variation, showing noticeable voltage dips and recovery delays.

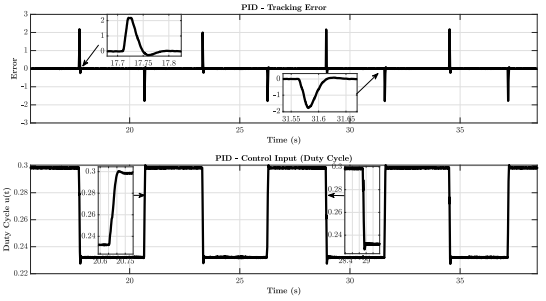

Fig. 13. PID error and control signal during input disturbance.

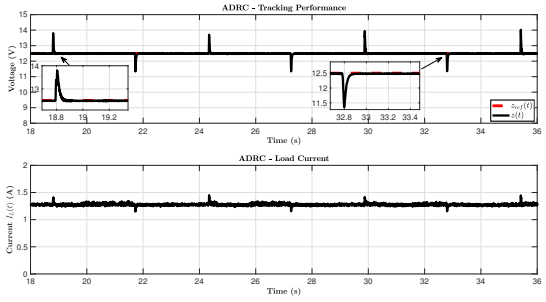

Fig. 14. ADRC's robust performance under input voltage variation.

In tracking performance (Fig. 6, 7, 8, 9, 10, 11), the PID controller exhibits reference voltage tracking with overshoots and oscillatory control inputs, consistent with simulations, while the ADRC achieves superior precision with no overshoot, near-zero tracking error, and smooth control adjustments. In contrast, the PD controller—lacking the disturbance compensation term $\hat{x}_3(t)$ from Eq. (22)—performs poorly, exhibiting significant steady-state error that highlights the critical role of disturbance estimation term.

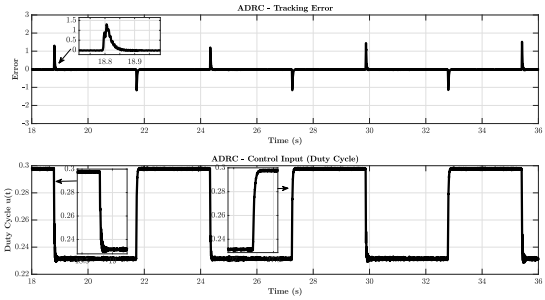

Fig. 15. ADRC's effective disturbance rejection, maintaining minimal error during input variation.

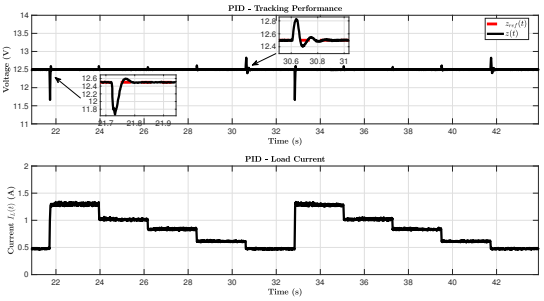

Fig. 16. Voltage and current response of the PID controller during load variation, showing the effect of load changes on regulation performance.

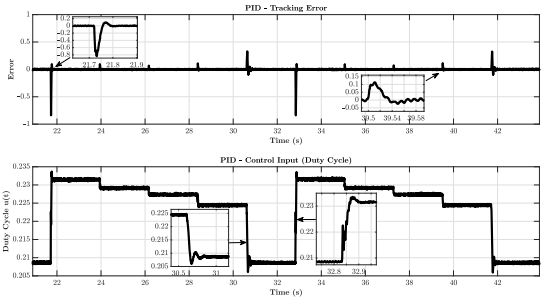

Fig. 17. PID tracking error large dips and recovery effort during load transient.

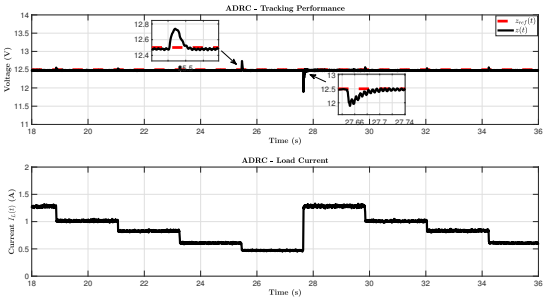

Fig. 18. ADRC's maintained voltage regulation under load variation.

Consequently, the PD controller was excluded from subsequent scenarios.

Under input voltage variations (Fig. 12, 13, 14, 15), the PID suffers from output deviations and abrupt tracking error spikes, whereas the ADRC maintains more stable output near the reference, demonstrating robust disturbance rejection. Similarly,

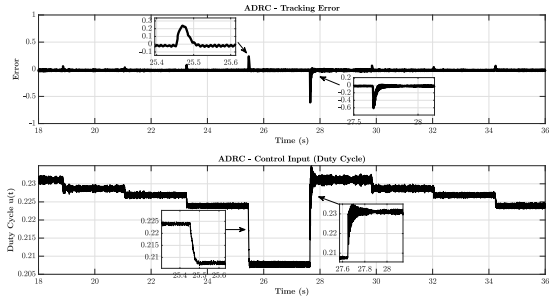

Fig. 19. ADRC's minimal error and robust control action during load change.

during load changes (Fig. 16, 17, 18, 19), the PID shows larger error spikes, while the ADRC limits voltage variations and sustains close to zero error. Across all tests, the ADRC outperforms the PID, combining faster response, minimal overshoot, and resilience to disturbances with smoother control efforts.

Table 4. Quantitative performance metrics for the three controllers under different scenarios.

Scenario	Controller	IAE	ISE	ITAE	Settling time (s)	Overshoot (%)
Tracking (S1)	PID	0.5021	3.1624	2.4713	0.0507	7.39
	PD	101.841	1421.63	505.485	0.0158	55.46
	ADRC	0.5850	0.4363	2.2190	0.0276	0.26
Input variation (S2)	PID	0.5356	0.5798	6.2500	0.0390	15.92
	ADRC	0.5312	0.1502	4.6977	0.0384	9.60
Load variation (S3)	PID	0.1768	0.0286	2.0005	0.0293	6.72
	ADRC	0.3668	0.0129	3.2991	0.027	4.86

The quantitative results in Table 4 further support these observations. ADRC consistently achieves the lowest ISE and negligible overshoot across all scenarios. In contrast, the PD controller yields extremely high error indices and excessive overshoot, confirming its inadequacy for this system. The PID controller delivers moderate performance, excelling in IAE and ITAE in some cases, but ADRC clearly provides the best overall trade-off between robustness, steady-state accuracy, and control effort.

The results confirm the superior numerical performance and underlying analytical advantages of the proposed ADRC. The controller's structure—based on total disturbance estimation and compensation—directly accounts for the observed voltage response, achieving a feedback-linearized control loop Eq. (23), where the nominal response is shaped through desired poles placement. Moreover, the disturbance rejection term introduces a generalized integral action that eliminates steady-state error.

Unlike the PID controller, whose fixed gains are sensitive to parameter drift and whose integral action only compensates for constant disturbances, ADRC inherently adapts to converter dynamics by estimating and rejecting lumped disturbances in real time. This extends compensation from constant to time-varying disturbances through dynamic estimation, resulting in smoother and more robust control behavior.

The strong agreement between theoretical predictions and experimental observations validates the proposed approach under the tested conditions, demonstrating its robustness for trajectory tracking and load regulation.

The practical implementation of ADRC, however, faces certain constraints. Its performance depends critically on the LESO, which involves a key trade-off: a high observer bandwidth improves disturbance rejection but also amplifies sensor noise, potentially causing control signal chatter. Furthermore, the stability guarantees assume that disturbances change at a bounded rate, which might not hold during sudden system faults. The reliance on a nominal input gain b_0 is another limitation, as large errors in this parameter can reduce the controller's effectiveness.

5. Conclusion

This paper presented a comprehensive study on the modeling, analysis, and robust control of a push–pull DC–DC converter using active disturbance rejection control. The proposed control law reduces the converter dynamics to a second-order integral form, ensuring precise voltage tracking and strong robustness under varying operating conditions. A Lyapunov-based analysis established the ultimate boundedness of the tracking and disturbance estimation errors, given appropriate bandwidth tuning of the observer and controller. Simulation results confirmed that ADRC outperforms PD and PID controllers in terms of tracking accuracy, disturbance rejection, and control smoothness under both input voltage and load variations.

Beyond this validation, the ADRC offers practical guidance for designing high-performance power supplies. Its ability to ensure robust voltage regulation under variable operating conditions makes it particularly suitable for applications like renewable energy conversion and electric vehicle systems, where inherent uncertainties and fast dynamics are important. While practical implementation considerations such as noise sensitivity and parameter uncertainties were discussed earlier, the developed flatness-based approach shows significant potential for next-generation converters. Future work will directly address the identified constraints by focusing on observer optimization under measurement noise and exploring robust tuning methods for varying operating conditions.

Data Availability Statement

Data sharing is not applicable to this article as no new data were created or analysed in this study.

Acknowledgement

The authors acknowledge the use of artificial intelligence tools (e.g., ChatGPT by OpenAI) for language editing and clarity improvement during the preparation of this manuscript. The authors are fully responsible for the scientific content, analysis, and conclusions.

References

[1] A. Hadjaissa, M. Benmiloud, K. Ameur, H. Bouchenak, and M. Dimeh, "Advanced photovoltaic emulator with ANN-Based modeling using a DC-DC push-pull converter and LQR control with current observer," *Iran. J. Electr. Electron. Eng.*, vol. 20, no. 4, 2024.

[2] A. Hendra, F. Hamada, and F. Yusivar, "Voltage control in push-pull DC-DC converter using state space averaging PID with soft-start for electric vehicle auxiliary system," in *2019 6th Int. Conf. Instrum., Control, Autom. (ICA)*, pp. 188–193, 2019.

[3] A. Kamath, "Push-pull converter simplifies isolated power supply design in HEV/EV systems," *Analog Des. J.*, vol. 10, pp. 1–6, 2020.

[4] J.-W. Lim, C. Bai, T. A. Wagaye, J.-H. Choi, and M. Kim, "Highly reliable push–pull resonant DC/DC converter for medium-power applications," *IEEE Trans. Ind. Electron.*, vol. 70, no. 2, pp. 1342–1355, 2023.

[5] M. Benmiloud, A. Hadjaissa, N. Abouchabana, K. Ameur, A. Benalia, and A. Rabhi, "Design and control of pv emulator based on DC-DC push-pull converter," in *2023 Int. Conf. Electr. Eng. Adv. Technol. (ICEEAT)*, vol. 1, pp. 1–6, 2023.

[6] S. Gorji, M. Ektesabi, and J. Zheng, "Isolated switched-boost push–pull DC/DC converter for step-up applications," *Electron. Lett.*, vol. 53, no. 3, pp. 177–179, 2017.

[7] K.-C. Tseng, I.-C. Li, and C.-A. Cheng, "Integrated buck and modified push-pull DC-DC converter with high step-down ratio," *IEEE Trans. Ind. Electron.*, vol. 67, no. 4, pp. 2681–2690, 2020.

[8] K. Khatun, V. R. Vakacharla, A. R. Kizhakkan, and A. K. Rathore, "Small signal analysis and control of snubberless naturally-clamped soft-switching current-fed push-pull DC-DC converter," *IEEE Trans. Ind. Appl.*, vol. 56, no. 4, pp. 3929–3943, 2020.

[9] H. Tarzamni, E. Babaei, F. P. Esmaeelnia, P. Dehghanian, S. Tohidi, and M. B. B. Sharifian, "Analysis and reliability evaluation of a high step-up soft switching push-pull DC-DC converter," *IEEE Trans. Rel.*, vol. 70, no. 1, pp. 1–14, 2020.

[10] Z. Ivanovic and M. Knezic, "Modeling push–pull converter for efficiency improvement," *Electron.*, vol. 11, no. 17, 2022.

[11] H. Zenk, "Comparison of the performance of photovoltaic power generation-consumption system with push-pull converter under the effect of five different types of controllers," *Int. J. Photoenergy*, vol. 2019, no. 1, p. 3810970, 2019.

[12] C. Trujillo, D. Velasco, E. Figueres, G. Garcerá, and R. Ortega, "Modeling and control of a push–pull converter for photovoltaic microinverters operating in island mode," *Appl. Energy*, vol. 88, no. 8, pp. 2824–2834, 2011.

[13] B. Rahmani and M. Belkheiri, "Adaptive neural network output feedback control for flexible multi-link robotic manipulators," *Int. J. Control*, vol. 92, no. 10, pp. 2324–2338, 2019.

[14] A. Izadbakhsh, A. Deylami, and S. Khorashadizadeh, "Observer-based versus non-observer based adaptive control of electrically driven cooperative manipulators using q-analogue of the bernstein-schurer-stancu operator as uncertainty approximator," *Int. J. Control Autom. Syst.*, vol. 21, no. 8, pp. 2664–2673, 2023.

[15] A. Izadbakhsh, A. A. Kalat, and S. Khorashadizadeh, "Observer-based adaptive control for hiv infection therapy using the baskakov operator," *Biomed. Signal Process. Control*, vol. 65, p. 102343, 2021.

[16] B.-Z. Guo and Z.-L. Zhao, *Active disturbance rejection control for nonlinear systems: An introduction*. John Wiley & Sons, 2017.

[17] S. B. Messaoud, M. Belkhiri, A. Belkhiri, and A. Rabhi, "Active disturbance rejection control of flexible industrial manipulator: A mimo benchmark problem," *Eur. J. Control*, vol. 77, p. 100965, 2024.

[18] S. Ahmad and A. Ali, "Active disturbance rejection control of DC-DC boost converter: A review with modifications for improved performance," *IET Power Electron.*, vol. 12, no. 8, pp. 2095–2107, 2019.

[19] Y. Yu, M. Kong, J. Yan, and Y. Lu, "Optimization strategy for output voltage of CCM flyback converter based on linear active disturbance rejection control," *Appl. Sci.*, vol. 13, no. 23, 2023.

[20] Z. Kang and Y. Li, "Active disturbance rejection control of full-bridge DC-DC converter for a pulse power supply with controllable charging time," *Electron.*, vol. 12, no. 24, p. 5018, 2023.

[21] R. Madonski, K. Łakomy, and J. Yang, "Simplifying ADRC design with error-based framework: case study of a DC–DC buck power converter," *Control Theory Technol.*, vol. 19, pp. 94 – 112, 2021.

[22] K. Łakomy, R. Madonski, B. Dai, J. Yang, P. Kicki, M. Ansari, and S. Li, "Active disturbance rejection control design with suppression of sensor noise effects in application to DC–DC buck power converter," *IEEE Trans. Ind. Electron.*, vol. 69, pp. 816–824, 2021.

[23] Y. Wang, S. Fang, and J. Hu, "Active disturbance rejection control based on deep reinforcement learning of pmsm for more electric aircraft," *IEEE Trans. Power Electron.*, vol. 38, no. 1, pp. 406–416, 2022.

[24] H. Sira-Ramirez, E. W. Zurita-Bustamante, and C. Huang, "Equivalence among flat filters, dirty derivative-based PID controllers, ADRC, and integral reconstructor-based sliding

mode control," *IEEE Trans. Control Syst. Technol.*, vol. 28, no. 5, pp. 1696–1710, 2019.

[25] H. Sira-Ramírez, A. Luviano-Juárez, M. Ramírez-Neria, and E. W. Zurita-Bustamante, *Active disturbance rejection control of dynamic systems: a flatness based approach*. Butterworth-Heinemann, 2017.

[26] G. Herbst and R. Madonski, *Active Disturbance Rejection Control: From Principles to Practice*. Springer Nature, 2025.

[27] Z. Nie, B. Zhang, Q. Wang, R.-J. Liu, and J.-L. Luo, "Adaptive active disturbance rejection control guaranteeing uniformly ultimate boundedness and simplicity," *Int. J. Robust Nonlinear Control*, vol. 30, pp. 7278 – 7294, 2020.

[28] S. Shao and Z. Gao, "On the conditions of exponential stability in active disturbance rejection control based on singular perturbation analysis," *Int. J. Control*, vol. 90, pp. 2085 – 2097, 2017.

[29] H. K. Khalil, "Nonlinear control," *IEEE Control Syst.*, vol. 35, no. Issue 6, pp. 281–84, 2015.